

Conditions on feature lines of two-dimensional scalar fields and their application to planar fluid flows

Balázs Sándor ^{a,*}, Péter Torma ^{a,b}

^a National Laboratory for Water Science and Water Security, Department of Hydraulic and Water Resources Engineering, Faculty of Civil Engineering, Budapest University of Technology and Economics, Műgyetem rkp. 3., H-1111 Budapest, Hungary

^b HUN-REN-SZTE Research Group for Photoacoustic Monitoring of Environmental Processes, Dóm tér 9, H-6720, Szeged, Hungary

ARTICLE INFO

Communicated by S. Wiggins

Keywords:

Contour lines

Feature lines

Two-dimensional scalar fields

Terrain objects

Planar fluid flows

Vorticity equations

ABSTRACT

We give a local algebraic condition on the coincidence of feature lines of contour curvature and slope (the latter is associated with ridges and valleys in a terrain map) for general two-dimensional scalar fields employing two newly derived feature lines. We also give a sufficient condition on the coincidence of feature lines using the reflection symmetries of the contour curves. We analyze the coincidence and separation of the different feature lines in symmetric and asymmetric terrain objects. Then, we apply the results for planar fluid flows, including simple ideal and viscous flows and a natural lake circulation. In the fluid dynamic examples, the stream function replaces the height field. The symmetry-breaking of the contour curves by boundary deformations and viscous dissipations are highlighted and discussed in each case.

1. Introduction

The geometric analysis of contour lines and other line-like objects (in other words, feature lines) has great importance in several applications. For example, two-dimensional (2D) scalar fields can describe terrain topographies and planar fluid flows. The feature lines of terrain maps can be associated with ridges and valleys of a terrain surface. Some of the first studies on terrain ridges and valleys come from Cayley [1] and Maxwell [2]. A significant result of these early studies is that not all ridge lines represent watershed divides, as they do not connect a maximum of the terrain with a saddle point [3]. The net of watershed divides defines drainage areas, where the water moves along slope lines of the terrain connecting maximum with minimum points [4].

The detection of ridges and valleys can be based on global and local methods [5]. For example, global methods are suitable for searching watershed divides as they consist of the location of the saddle points and integration from these points along the gradient field. Local methods provide feature lines as manifolds solving algebraic equations for the height field and its derivatives. A detailed mathematical description of the height field as an explicitly written surface has been obtained, and invariants have been deduced by Koendreink and van Doorn [6]. Some invariants are admitted for rescaling of heights, while others belong to affine transformations of the plane [6]. A superset of feature lines can be captured using local methods, including ridges and valleys without saddle connection and special fields, for example,

locally flat areas. A local condition for ridges has been given by de Saint-Venant [7] as the locus of points with minimal slope along a height contour (or isohypse). A necessary condition for the feature lines can be obtained locally by formulating general conditions on parallel vectors [3,5]. The formalism that Peikert and coworkers used led to a relative extrema condition for an arbitrary scalar field with respect to a height field.

The applicability of feature lines goes far beyond terrain analysis [6] to digital image processing [8] and hydrodynamics [5]. Features lines of flow fields already provide a valuable tool for hydrodynamic analysis with several applications. For example, flow separation and attachment lines were detected and discussed with parallel vector conditions in 2D flows [5,9]. Furthermore, ridges of passive scalars have been used to extract statistical information in small-scale turbulent flows [10,11]. In oceanography, coherent structures of flow fields can be detected and analyzed employing the so-called finite-time Lyapunov exponent (FTLE). In the case of unsteady 2D flows, the ridges of the FTLE field can directly be associated with the flow field's different feature lines [12]. However, Lagrangian coherent structures should be distinguished from the Lyapunov exponent ridges [13]. In [14], the ridges of the scalar field of the angles between line elements in the flow were used for flow visualization purposes. In three-dimensional (3D) hydrodynamics, we see examples of ridge-based detection of separation patterns in connection to the wall-vorticity and skin-friction fields [15],

* Corresponding author.

E-mail address: sandor.balazs@emk.bme.hu (B. Sándor).

which was argued in [16] by developing an exact separation theory based on mass conservation. In 3D flows, feature lines of vorticity and pressure fields are commonly used to define vortex cores [17–19]; however, a Lagrangian definition of a vortex (as a material tube) is also available [20] with more general invariant properties than the vortex core defined by the ridge-based methods.

In this paper, we give a local algebraic condition on the coincidence of the feature lines of contour curvature and slope (the latter is associated with the ridges and valleys) for general 2D scalar fields. Our motivation was that intuitively, on a terrain map, the point of maximal contour curvature along a height contour, or in other words, isohypse, coincides with a ridge or valley point on the same isohypse. Intuitively, the feature lines of extremal contour curvature and extremal slope coincide. It was shown by an example – first introduced in the XIX. century [21] – that the previous statement is not generally true [5]. The feature lines of the extremal contour curvature and extremal slope do not necessarily coincide. However, the example is an artificial height field given by the surface points of an inclined elliptic cylinder. To our knowledge, the coincidence or separation of curvature and slope feature lines has not been analyzed yet for arbitrary 2D scalar fields. Our condition involves the definition of two further feature lines. After deriving the coincidence condition in general, we derive a sufficient condition on the coincidence using the reflection symmetries of the isohypse curves. We show some examples referring to simple terrain objects and then apply the results for planar fluid flows as a novelty. The stream function replaces the height field, so the streamlines play the role of the isohypses. We analyze the coincidence and separation of the different feature lines in 2D flows of different complexity, from Eulerian to simple viscous flows. Finally, we derive the feature lines in a natural lake flow to analyze the large-scale circulation pattern as a potential application field.

2. Poisson brackets on 2D scalar fields

Let $\psi(x, y)$ and $\phi(x, y)$ be scalar fields.

Definition 1. The Poisson bracket of ψ and ϕ is

$$\{\psi, \phi\} = \frac{\partial \psi}{\partial x} \frac{\partial \phi}{\partial y} - \frac{\partial \psi}{\partial y} \frac{\partial \phi}{\partial x}. \quad (1)$$

Let Ω be a simply connected planar domain. If

$$\{\psi, \phi\} \Big|_{x=x^*, y=y^*} = 0, \quad (2)$$

moreover $\nabla \psi \neq \mathbf{0}$ and $\nabla \phi \neq \mathbf{0}$, then the contour lines of ψ and ϕ have first-order contact at $(x^*, y^*) \in \Omega$. Condition (2) can be interpreted also as follows:

$$\nabla \psi = c \nabla \phi, \quad \frac{\nabla \psi \cdot \nabla \phi}{|\nabla \psi| |\nabla \phi|} = \pm 1, \quad (3)$$

where c is a constant,

$$\nabla \psi \cdot \nabla \phi = \frac{\partial \psi}{\partial x} \frac{\partial \phi}{\partial x} + \frac{\partial \psi}{\partial y} \frac{\partial \phi}{\partial y} \quad (4)$$

is the dot product of the gradient fields, while $|\nabla \psi|$ and $|\nabla \phi|$ are the gradient vector magnitudes. Eq. (2) also holds where one of the fields has a critical point, i.e., $\nabla \psi = \mathbf{0}$, or $\nabla \phi = \mathbf{0}$.

Let $l_\phi \subset \Omega$ be the set of such points as

$$l_\phi = \{(x, y) : \{\psi, \phi\} = 0\}, \quad l_\phi \subset \Omega, \quad (5)$$

where the $\{\}$ bracket defines the set. This set of points typically describes a curve, i.e., the implicit curve (the zero contour) of the scalar field $\{\psi, \phi\}$. Fig. 1 shows a possible configuration for l_ϕ . Here (x_1^*, y_1^*) is an extremal point of ψ , (x_2^*, y_2^*) and (x_3^*, y_3^*) represent first-order contact points between ψ and ϕ , and (x_4^*, y_4^*) is a saddle point of ψ . The first-order contact points can be interpreted as constrained relative extrema as well: there is a relative extremum of ϕ at the points (x_2^*, y_2^*) and (x_3^*, y_3^*) , constrained to the curves $\psi = \psi_2$ and $\psi = \psi_3$, respectively.

The l_ϕ curve can also contain higher-order contact points between ψ and ϕ , which are not denoted in Fig. 1. Without giving higher-order conditions, l_ϕ is the superset of critical points, first-order contact points, and higher-order contact points. We call such l_ϕ implicit curves to raw feature lines [3]. The elements of the subset of l_ϕ not containing higher-order contact points are called extremal lines.

We extend the zero condition of the Poisson brackets from points (2) and curves (5) to the whole Ω domain as

$$\{\psi, \phi\} = 0, \quad \forall (x, y) \in \Omega. \quad (6)$$

This condition ensures that the contours of ψ and ϕ coincide everywhere in Ω . The graphical interpretation of conditions (5) and (6) can be seen on the left and right panels of Fig. 2, respectively. The nonexistence of the implicit curve l_ϕ follows from the vanishing condition (6).

3. Coincidence of the raw feature lines of slope and contour curvature fields

In the first part of this Section, after defining derivative fields of ψ with the corresponding raw feature lines, we give a local algebraic condition on the coincidence of the raw feature lines of slope and contour curvature, which will involve defining two further feature lines. We use the terminology of terrain analysis to interpret the definitions and our results.

Let Ω be the map of a terrain field. Then ψ describes the height field of the terrain. We introduce the following scalar fields:

$$\sigma = |\nabla \psi|, \quad (7)$$

$$\chi = |\nabla \sigma|, \quad (8)$$

$$\omega = \nabla \cdot (\nabla \psi) = \Delta \psi, \quad (9)$$

$$\kappa = \nabla \cdot \left(\frac{\nabla \psi}{|\nabla \psi|} \right) = \frac{\omega}{\sigma} - \frac{\nabla \psi \cdot \nabla \sigma}{\sigma^2}. \quad (10)$$

Eqs. (7)–(8) define the slope of ψ and the slope of the slope field of ψ , respectively; the latter we call to second-order slope. Eqs. (9)–(10) are the Laplacian of ψ , and the contour curvature (or plan curvature) field of ψ [22], respectively. The Laplacian and the contour curvature refer to the convergence or divergence of the slope lines, as can be seen by comparing their first expressions in Eqs. (9) and (10), respectively. The more uniform slope field results in the closer relation between the Laplacian and contour curvature fields.

We define the following raw feature lines:

$$l_\sigma = \{(x, y) : \{\psi, \sigma\} = 0\}, \quad l_\sigma \subset \Omega, \quad (11)$$

$$l_\chi = \{(x, y) : \{\psi, \chi\} = 0\}, \quad l_\chi \subset \Omega, \quad (12)$$

$$l_\omega = \{(x, y) : \{\psi, \omega\} = 0\}, \quad l_\omega \subset \Omega, \quad (13)$$

$$l_\kappa = \{(x, y) : \{\psi, \kappa\} = 0\}, \quad l_\kappa \subset \Omega. \quad (14)$$

If the raw feature line of the slope, l_σ , connects a saddle and an extremum of ψ with first-order contact points (as we see in Fig. 1 with l_ϕ), then l_σ is a watershed divide. First-order contact points without saddle and extremum connection can also form ridges or valleys of ψ [3]. The higher-order contact points are locally flat spots of the height field described by ψ . The terrain has a uniform slope (constant slope along each isohypse) everywhere in Ω if the vanishing condition (6) between ψ and σ and the configuration drawn on the right panel of Fig. 2 holds.

As ridge or valley lines are extremal slope lines and the extremal contour curvature lines refer to extremal convergence or divergence of the slope lines, one can have the intuition that those lines may coincide. However, they do not coincide in general as counter-examples – [5,21] – have shown that. In the following, we give a local sufficient condition on the coincidence of the raw feature lines of the slope and the contour curvature fields, which involve the contribution of the raw feature lines of the second-order slope and the Laplacian.

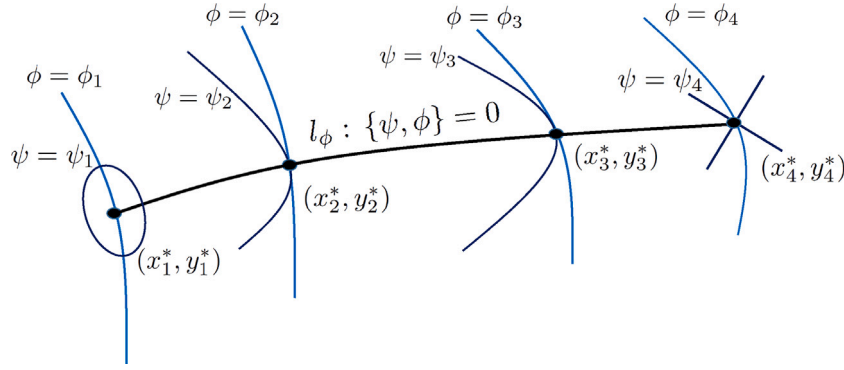


Fig. 1. A configuration of l_ϕ , as an extremal line of ϕ , between an extremum and a saddle of ψ .

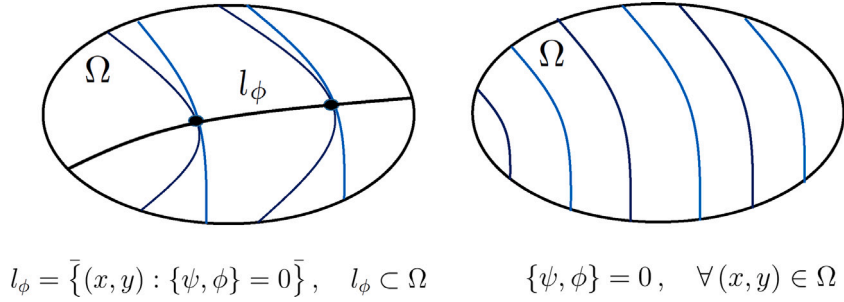


Fig. 2. The implicit curve l_ϕ versus everywhere vanishing Poisson bracket.

Theorem 2. A sufficient condition on the coincidence of the raw feature lines of slope and contour curvature is the coincidence of the raw feature lines of slope and second-order slope, and the coincidence of the raw feature lines of slope and Laplacian. Consequently, the intersection set of the raw feature lines of slope and contour curvature is equal to the intersection set of the raw feature lines of slope, second-order slope, Laplacian, and contour curvature,

$$l_\sigma \cap l_\kappa = l_\sigma \cap l_\chi \cap l_\omega \cap l_\kappa, \quad (15)$$

Proof. The intersection set of the raw feature lines of slope and contour curvature (as sets of points) defines the domain where they coincide. We can write using Eqs. (11) and (14) that

$$l_\sigma \cap l_\kappa = \{(x, y) : \{\psi, \sigma\} = \{\psi, \kappa\} = 0\}. \quad (16)$$

The Poisson bracket of the scalar field ψ and its scalar contour curvature field κ by applying the right-hand side of Eq. (10) reads as

$$\{\psi, \kappa\} = \frac{1}{\sigma} \{\psi, \omega\} - \frac{\omega}{\sigma^2} \{\psi, \sigma\} - \frac{1}{\sigma^2} \{\psi, \nabla \psi \cdot \nabla \sigma\} + \frac{\nabla \psi \cdot \nabla \sigma}{\sigma^4} \{\psi, \sigma^2\}. \quad (17)$$

It follows from condition

$$\{\psi, \sigma\} = 0 \quad (18)$$

that

$$\{\psi, \sigma^2\} = 0, \quad (19)$$

$$\nabla \psi \cdot \nabla \sigma = \sigma \chi, \quad (20)$$

$$\{\psi, \nabla \psi \cdot \nabla \sigma\} = \sigma \{\psi, \chi\}. \quad (21)$$

Substituting the last four Equations into Eq. (17) results $\{\psi, \kappa\}$ along the raw feature line l_σ :

$$\{\psi, \kappa\} = \frac{1}{\sigma} \{\psi, \omega\} - \frac{1}{\sigma} \{\psi, \chi\}, \quad (22)$$

and so

$$l_\sigma \cap l_\kappa = \{(x, y) : \sigma \{\psi, \sigma\} = \{\psi, \omega\} - \{\psi, \chi\} = 0\}. \quad (23)$$

The sufficient condition on the coincidence of the raw feature lines of slope and contour curvature, as stated in Theorem 2 is satisfied if all the three terms of Eq. (22) are zero, which leads to Condition (15) as well. \square

In the following part of this Section, we deduce a sufficient condition on the coincidence of the raw feature lines (11)–(14) involving reflection symmetries of the isohypse curves. We start with two isohypse configurations possessing infinite symmetry axes and no raw feature lines. We define the isohypses as parallel, straight lines or concentric circles in Ω , with

$$\psi = f(y + cx), \quad (24)$$

and

$$\psi = g(x^2 + y^2), \quad (25)$$

respectively.

Applying the vanishing condition of the Poisson bracket in Ω , (6) on Eqs. (24) and (25) by using Eqs. (7)–(10) for σ , χ , ω , κ and substituting them in ϕ results

$$\{\psi, \sigma\} = 0, \{\psi, \chi\} = 0, \{\psi, \omega\} = 0, \{\psi, \kappa\} = 0, \quad \forall (x, y) \in \Omega. \quad (26)$$

The terrain objects described by Eq. (24) have straight isohypses everywhere, the surface curves perpendicular to the isohypses are congruent objects, and the surface has continuous translational symmetry along the isohypses. The terrain objects described by Eq. (25) represent circular hills with continuous rotational symmetry. None of the raw feature lines (11)–(14) exist in any of the fields defined by Eqs. (24)–(25). Let T denote a reflection symmetry axis. The terrain object described by Eqs. (24) and (25) possesses an infinite number of symmetry axes, as seen on the left and right panels of Fig. 3, respectively.

Theorem 3. Suppose that there are raw feature lines $l_\sigma \subset \Omega$, $l_\chi \subset \Omega$, $l_\omega \subset \Omega$, $l_\kappa \subset \Omega$. Let T_i , $i = 1 \dots n$ denote the reflection symmetry axes of the isohypse curves where n is finite, and T_i is not an isohypse. Then, the

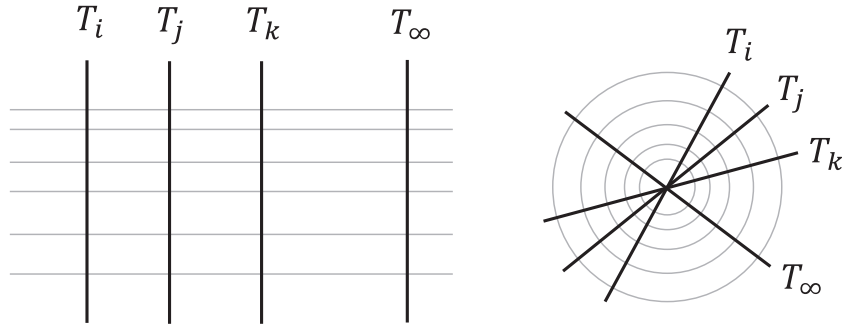


Fig. 3. Straight (left panel) and circular (right panel) isohypses (solid grey lines) with an infinite number of reflection symmetry axes (solid black lines).

union set of the symmetry axes is a subset of the intersection set of the raw feature lines:

$$\bigcup_{i=1}^n T_i \subseteq l_\sigma \cap l_\chi \cap l_\omega \cap l_\kappa. \quad (27)$$

Moreover, the raw feature lines in the intersection set are extremal lines.

Proof. The T_i symmetry axis can be positioned arbitrarily. The coordinate axes can be transformed by a continuous translation and rotation so that one of them coincides with T_i . Let the new coordinates be ξ and η , and let the isohypses have reflection symmetry with respect to the η axis, so ψ is an even function with respect to the ξ coordinates:

$$\psi(-\xi, \eta) = \psi(\xi, \eta). \quad (28)$$

Substituting Eq. (28) into Eqs. (7)–(10) turns out that if ψ is an even function, then so are its derived fields,

$$\sigma(-\xi, \eta) = \sigma(\xi, \eta), \quad (29)$$

$$\chi(-\xi, \eta) = \chi(\xi, \eta), \quad (30)$$

$$\omega(-\xi, \eta) = \omega(\xi, \eta), \quad (31)$$

$$\kappa(-\xi, \eta) = \kappa(\xi, \eta). \quad (32)$$

If neither the isohypses nor the contours of the derived fields are straight lines, then all the scalar fields have to have constrained relative extrema along the η symmetry axis, with respect to the $\eta = \text{const.}$ coordinate lines. In other words, first-order contact points exist between all five scalar fields, and the $\eta = \text{const.}$ coordinate lines, i.e.

$$\{\psi, \eta\} \Big|_{\xi=0} = 0, \quad (33)$$

$$\{\sigma, \eta\} \Big|_{\xi=0} = 0, \quad (34)$$

$$\{\chi, \eta\} \Big|_{\xi=0} = 0, \quad (35)$$

$$\{\omega, \eta\} \Big|_{\xi=0} = 0, \quad (36)$$

$$\{\kappa, \eta\} \Big|_{\xi=0} = 0, \quad (37)$$

where the Poisson brackets executed in (ξ, η) coordinates. It follows from Eqs. (33)–(37) that

$$\{\psi, \sigma\} \Big|_{\xi=0} = 0, \quad (38)$$

$$\{\psi, \chi\} \Big|_{\xi=0} = 0, \quad (39)$$

$$\{\psi, \omega\} \Big|_{\xi=0} = 0, \quad (40)$$

$$\{\psi, \kappa\} \Big|_{\xi=0} = 0. \quad (41)$$

The Poisson brackets have to take zero values at $\xi = 0$, i.e., along the symmetry axis T_i (which coincides with the η axis). This completes the proof of Theorem 3: there are coinciding extremal lines along the symmetry axis T_i , and the method can be repeated for every symmetry axis, which finally results in Statement (27). \square

We illustrate the results with a few examples. Fig. 4 shows three saddles with two, one, and zero symmetry axes from the left to the right, respectively. The symmetry axes – as stated in Theorem 3 – are related to reflection symmetries of the isohypse curves and perpendicular to the isohypse curves. On the left panel are four symmetry axes of the isohypses (l_κ coincides with all of them), but only two cross the isohypses perpendicularly. Those serve as the common intersection of the raw feature lines, i.e., where they coincide. There are only two raw feature lines because two Poisson brackets are zero on the whole plane. The equations of the isohypses, the zero Poisson-bracket fields, and the coinciding conditions are

$$\psi = x^2 - y^2,$$

$$\{\psi, \chi\} = 0, \quad \{\psi, \omega\} = 0, \quad \forall (x, y) \in \Omega$$

$$T_1 \cup T_2 = l_\sigma \cap l_\kappa. \quad (42)$$

In the middle panel of Fig. 4, one symmetry axis is broken compared to the saddle in the left panel. Four feature lines coincide along the symmetry axis. The raw feature line of the contour curvature, l_κ , detaches from the broken vertical symmetry axis and intersects with l_σ in the saddle. The raw feature lines of the slope and the second order slope, l_σ , and l_χ lie on the broken vertical symmetry axis. The equation of the isohypses and the coinciding condition read as

$$\psi = x^2 - y^2 + x^3,$$

$$T_1 = l_\sigma \cap l_\chi \cap l_\omega \cap l_\kappa. \quad (43)$$

On the right panel of Fig. 4, a sine function is added to the saddle,

$$\psi = x^2 - y^2 + \sin(xy). \quad (44)$$

As a result, there are no symmetry axes and coinciding feature lines.

Fig. 5 shows an equilateral triangle-based domain on the left panel, with three symmetry axes of the isohypse curves, which are the symmetry axes of the domain, too. The scalar field ψ – the equation of the isohypses – is constructed as the product of the implicit curves describing the sides of the domain. The height field's extremum point coincides with the triangle's centroid. The corners of the triangle are saddles of the height field. The equations of the isohypses, the zero Poisson-bracket fields, and the coinciding conditions are

$$\psi = y(\sqrt{3}x - y)(\sqrt{3} - \sqrt{3}x - y),$$

$$\{\psi, \omega\} = 0, \quad \forall (x, y) \in \Omega$$

$$T_1 \cup T_2 \cup T_3 = l_\sigma \cap l_\chi \cap l_\kappa. \quad (45)$$

On the right panel of Fig. 5, we see a triangle domain with zero symmetry axes constructed from the equilateral triangle with a clockwise rotation of its left edge. The equation of the isohypses is

$$\psi = y \left(\frac{x}{\sqrt{3}} - y \right) (\sqrt{3} - \sqrt{3}x - y). \quad (46)$$

Compared to the equilateral case, all three symmetry axes are broken, and all the raw feature lines are separated. However, the medians of

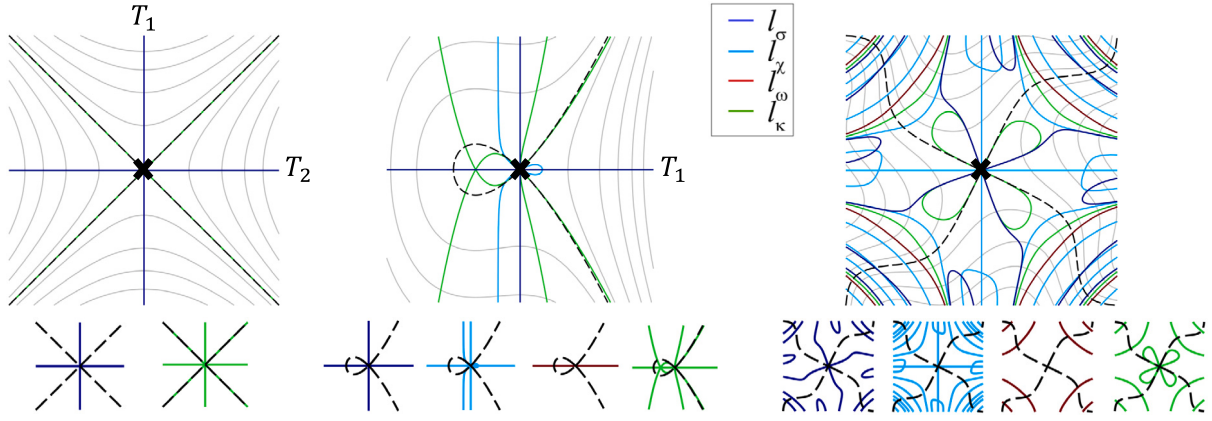


Fig. 4. Isohypse curves (solid grey lines) and raw feature lines (according to the legend) for the symmetric (left and middle panels) and asymmetric (right panel) saddles. The dashed black lines denote zero isohypses. The black crosses denote the saddle points.

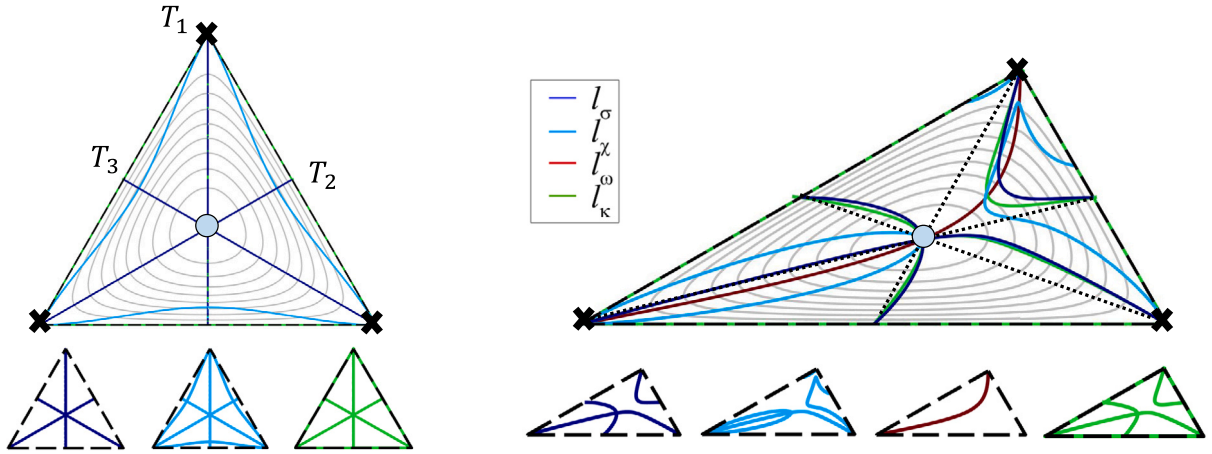


Fig. 5. Isohypse curves (solid grey lines) and raw feature lines (according to the legend) for the symmetric (left panel) and asymmetric (right panel) triangular terrain objects. The dashed black lines denote zero isohypses, which form the boundary of the terrain object. The black crosses and the blue circles denote the saddles (corners) and the extrema (centroids), respectively. On the right panel, the black dots denote the median lines of the triangle.

the triangle play an important role. The raw feature lines of slope and contour curvature, l_σ , and l_k can be resolved in three subsets. One intersects with the medians at one edge of the triangle (saddle point of the isohypses) and at the middle of a side, one at two edges and the centroid, and one at the middle of two sides and the centroid. The subset of lines that do not cross the centroid is connected with the edge of the obtuse angle. The subsets of lines connecting the edges of acute angles and the middle of the two longest sides cross the centroid. The raw feature line of the second-order slope, l_χ , shows a more general pattern than l_σ and l_k . However, a subset intersects with the medians on two edges and the centroid. Only one curve represents the raw feature line of the Laplacian, l_ω , which intersects with the medians in two edges and the centroid.

Fig. 6 shows a square-based, symmetric isohypse configuration on the left panel. The scalar field is constructed by the product of the implicit curves representing the square. The height field's extremum point coincides with the square's centroid. The corners of the square are saddles of the height field. The equations of the isohypses and the coinciding conditions are

$$\psi = xy(x-1)(y-1),$$

$$T_1 \cup T_2 \cup T_3 \cup T_4 = l_\sigma \cap l_\chi \cap l_\omega \cap l_k. \quad (47)$$

We break all four symmetry axes by transforming the square into trapezoids by rotating the lower horizontal side counter-clockwise with two different angles. The new isohypse fields are described by

$$\psi = x(y-0.1x)(x-1)(y-1), \quad (48)$$

and

$$\psi = x(y-0.4x)(x-1)(y-1), \quad (49)$$

and they are shown in the middle and the right panels of Fig. 6, respectively. The bimedial line joining the midpoints of the two parallel, vertical sides contains the centroid of the trapezoid. The raw feature lines of slope and contour curvature, l_σ , and l_k intersect at these midpoints. The raw feature line pattern l_σ and l_k in the trapezoid with the smaller rotation angle shows a uniform picture: there are four subsets, all of them detached from the centroid and connect a corner with an edge (at the midpoint of the edges). The raw feature lines of the second-order slope and Laplacian, l_χ , and l_ω have distinct pictures at the obtuse angle of the trapezoid. In the trapezoid with the larger rotation angle, the obtuse angle becomes larger, and the acute angle becomes smaller compared to the previous case. The bimedial line between the midpoints of the vertical sides still intersects with l_σ and l_k . However, they show a different picture: at the quadrant of the trapezoid belonging to the acute angle, their pattern is similar to the one around the acute angle of the asymmetric triangle shown in the right panel of Fig. 5.

We summarize a few observations on the raw feature line patterns based on the simple examples of the saddles and the circular isohypses with an extremum of the centroid of triangular and quadrilateral domains. First, as Theorem 3 indicated, the coinciding feature lines along an isohypse symmetry axis are separated once the symmetry axis is broken. Then the raw feature lines of slope and contour curvature, l_σ

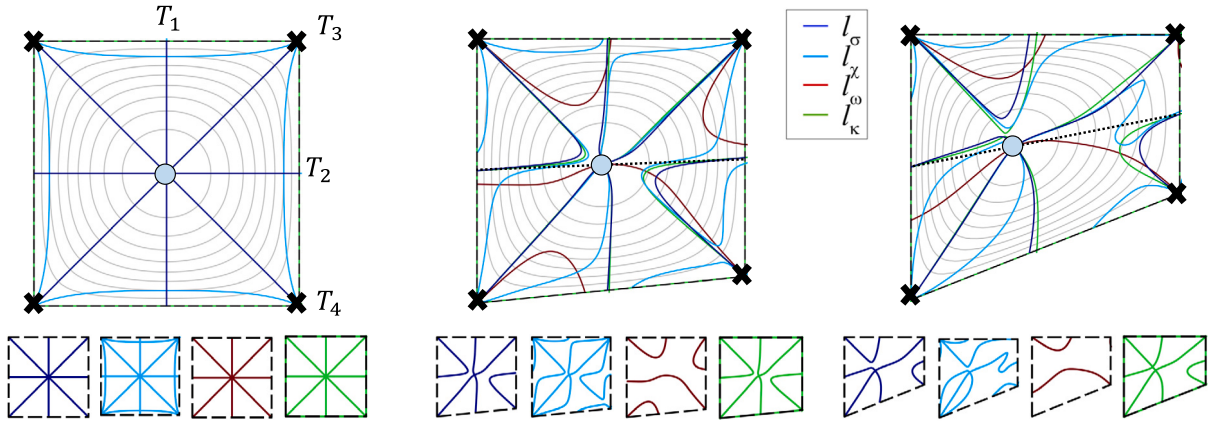


Fig. 6. Isohypse curves (solid grey lines) and raw feature lines (according to the legend) for the symmetric (left panel) and asymmetric (middle and right panels) quadrilateral terrain objects. The dashed black lines denote zero isohypses, which form the boundary of the terrain object. The black crosses and the blue circles denote the saddles (corners) and the extrema (centroids), respectively. On the middle and right panels, the black dots denote the bimedians of the trapezoids.

and l_κ usually stay closer to each other than to the raw feature lines of the second-order slope and Laplacian, l_χ and l_ω . In the triangular and quadrilateral examples, the connection of corners and centroids of the bounding polygon (saddles and extrema of the isohypse field) by various raw feature lines strongly depends on the geometric features of the polygon, i.e., on median or bimedians and the magnitude of the angles. The raw feature line of the Laplacian, l_ω , shows the highest sensitivity to the symmetry-breaking. These lines separate to the most significant distance from the broken symmetry axes and show the highest variability and nonuniform behavior.

To conclude, realistic topographies usually do not have isohypse fields with reflection symmetries. Their raw feature lines may not coincide in most cases. Moreover, the boundaries of natural terrain objects are usually not straight lines, which can result in more general variability of the raw feature line patterns.

In the next Section, we apply the results to describe planar fluid flows involving fluid dynamic equations. These equations will be related to the Poisson bracket $\{\psi, \omega\}$ and the raw feature lines l_ω , which has shown the highest sensitivity to the geometric circumstances. By the fluid dynamic equations, the geometric (kinematic) constraints will be accompanied by dynamic ones. The effects of such constraints will be discussed, as the description of planar ideal and viscous flows in the view of Theorems 2 and 3.

4. Application to planar fluid flows

We present the first application of the coincidence condition of the raw feature lines (15) and the coincidence condition of the extremal lines with the symmetry axes (27) on 2D hydrodynamics in order to identify kinematic and dynamic effects with feature line patterns. All four different feature lines, which were defined by Eqs. (11)–(14) have direct hydrodynamic meaning.

Up to this section, we considered ψ as a 2D scalar field describing terrain topographies. If a water particle runs down on a terrain, it moves along the slope lines of the field perpendicularly to the contours of ψ (to the isohypses). Now, ψ plays the role of the stream function of the flow, and the contours of ψ are the streamlines. We consider steady flows, meaning that streamlines are orbits of fluid elements. The slope of the terrain, σ , defined by Eq. (7), is the velocity magnitude of the flow, while the second-order slope, χ – Eq. (8) – is the velocity gradient magnitude. The Laplacian of the field – ω , given by Eq. (9) – is the scalar vorticity. The new interpretation of the convergence or divergence of slope lines is the local angular velocity of a fluid element. The contour curvature, κ , Eq. (10), is streamline curvature now.

The raw feature lines contain extremal lines as a subset. There is hydrodynamic meaning beyond the extremal lines. The impulse transport is extremal across the extremal lines of the velocity magnitude.

Along the extremal line of the velocity gradient magnitude, the shear is extremal; consequently, the mixing properties are extremal across the line. The extremal line of vorticity has a dynamic feature beyond the extremal angular velocity in connection to the viscous dissipation.

In the following, we discuss the circumstances of the fulfillment of conditions (15) and (27) for ideal and viscous fluids, using the vorticity form of the 2D Euler and Navier–Stokes equations, respectively, on the simply connected planar domain Ω .

4.1. Application to ideal fluids

The stream function $\psi(x, y)$ and vorticity $\omega(x, y)$ form of the Euler equation of the steady flow of an ideal fluid in two dimensions [23,24] is

$$\{\psi, \omega\} = 0, \quad \forall (x, y) \in \Omega. \quad (50)$$

The geometric meaning of Eq. (50) is that the contours of ψ and ω – i.e., the streamlines and the isovortical lines – coincide everywhere in Ω . Consequently, there are no raw feature lines of vorticity in ideal fluid flows. The Euler vorticity Eq. (50) is the vanishing condition (6) of the Poisson bracket of the stream function and the vorticity in Ω , a dynamic constraint with kinematic interpretation.

Proposition 4. *Theorem 3 can be applied supposing $T_i, i = 1 \dots n$ reflection symmetry axes of the streamline pattern, where n is finite and T_i is not a streamline. Then*

$$\bigcup_{i=1}^n T_i \subseteq l_\sigma \cap l_\chi \cap l_\kappa. \quad (51)$$

The extremal lines of velocity magnitude, velocity gradient magnitude, and streamline curvature coincide along the T_i reflection symmetry axes of the streamline pattern for the steady, planar flow of an ideal fluid satisfying the vorticity Eq. (50). In other words, extremal impulse transport, velocity gradient, and streamline curvature take place at the same points along a streamline: at the intersection points with such symmetry axes.

We analyze the raw feature lines for a circular flow in an equilateral cell of unity length. The stream function which describes such a flow is [23]

$$\psi = \sin(\pi x) \sin(\pi y), \quad \Omega = [0, 1] \times [0, 1], \quad (52)$$

which satisfies the vorticity Eq. (50) and has the following coinciding condition:

$$\{\psi, \omega\} = 0, \quad \forall (x, y) \in \Omega, \quad T_1 \cup T_2 \cup T_3 \cup T_4 = l_\sigma \cap l_\chi \cap l_\kappa. \quad (53)$$

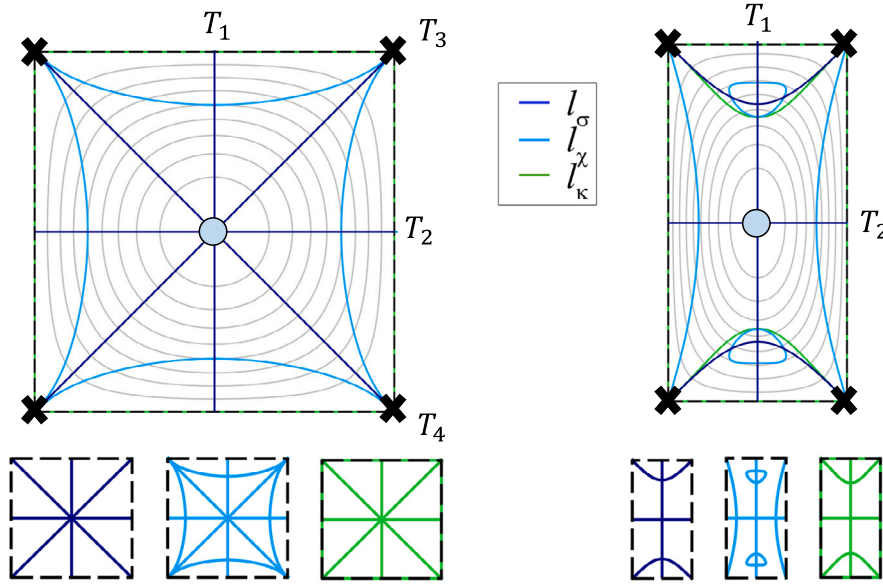


Fig. 7. Streamlines (solid grey lines) and raw feature lines (according to the legend) for the cellular flows described by Eqs. (52) and (54) on the left and right panels, respectively. The dashed black lines denote zero streamlines, which form the boundary of the flow field. The black crosses and the blue circles denote the saddles and the extrema, respectively.

The feature lines coincide along the streamline pattern's four symmetry axes, as seen on the left panel of Fig. 7.

We construct a new stream function from Eq. (52) by a symmetry-breaking scaling transformation as

$$\psi = \sin(2\pi x) \sin(\pi y), \quad \Omega = [0, 0.5] \times [0, 1], \quad (54)$$

with which

$$\{\psi, \omega\} = 0, \quad \forall (x, y) \in \Omega, \quad T_1 \cup T_2 = l_\sigma \cap l_\chi \cap l_\kappa. \quad (55)$$

The diagonal symmetry axes are dismissed, and the raw feature lines along the diagonals are separated. However, there are still horizontal and vertical symmetry axes with coinciding raw feature lines. The results are shown on the right panel of Fig. 7. The separated feature lines have detached from the central extremum of the stream function compared to the ones covering the diagonal symmetry axes. The separation of the feature lines completely resulted from the break of the symmetry axes and the flow pattern, i.e., from pure kinematic reasons. We note that a uniform (equivalent in both axes) scaling transformation would have preserved not only the streamline pattern but also the pattern of the raw feature lines; because of the scaling symmetry of the equation and the raw feature lines. In the following, we consider viscous dissipation effects by replacing the ideal fluid with a real one, and so the Euler equation with the Navier–Stokes equation.

4.2. Application to viscous fluids

The stream function $\psi(x, y)$ and vorticity $\omega(x, y)$ form of the Navier–Stokes equation of the steady, planar flow of a viscous fluid [23,24] is

$$\{\psi, \omega\} = \frac{1}{\text{Re}} \Delta \omega, \quad \forall (x, y) \in \Omega \quad (56)$$

where Re is the Reynolds number. At each point of Ω , the intersection angle between the streamlines and isovortical lines is proportional to the Laplacian of the vorticity. Restricting to laminar flows, the right-hand side of Eq. (56) expresses the effect of viscous dissipations as the curl of the dissipation force resulting from shear stresses. The raw feature lines of the vorticity $-l_\omega$, Eq. (13) – appear in the flows driven by the vorticity Eq. (56), compared to the ideal flows. Along those

feature lines, the curl of the dissipation force is vanishing according to the right-hand side of Eq. (56). Let L denote the

$$L = \{(x, y) : \Delta \omega = 0\}, \quad L \subset \Omega \quad (57)$$

set of points, i.e., the implicit curve of the viscous dissipation.

Proposition 5. *It follows from the vorticity Eq. (56) that the raw feature line of vorticity coincides with the implicit curve of the viscous dissipation,*

$$l_\omega = L. \quad (58)$$

The appearance of the curl of the viscous dissipation force via the right-hand side of the vorticity Eq. (56) has brought a dynamic constraint to the raw feature line pattern and so to the conditions of their coincidence. Consequently, the viscous dissipation can cause further symmetry-breaking effects in the raw feature line pattern. This fact agrees with the nature of the 2D Navier–Stokes equation, where the vorticity is not a conserved quantity compared to the 2D Euler equation [24].

Proposition 6. *The streamline pattern of the steady, planar flow of a viscous fluid satisfying the vorticity Eq. (56) does not possess a finite number of reflection symmetry axes which are not streamlines. Consequently, extremal values of velocity magnitude, velocity gradient magnitude, vorticity, and streamline curvature cannot coincide in such a way that Theorem 3 states.*

We prove this statement above indirectly. Let us suppose that there are reflection symmetry axes denoted by T_i . Transforming the coordinate system into the (ξ, η) coordinates where ξ is placed alongside the T_i symmetry axes, the stream function is an even function with respect to the ξ coordinate (Eq. (28)):

$$\psi(\xi, \eta) = \psi(-\xi, \eta). \quad (59)$$

This assumption leads to a contradiction, namely, the left- and right-hand sides of the vorticity equation have different parity (56):

$$\{\psi(\xi, \eta), \omega(\xi, \eta)\} = -\{\psi(-\xi, \eta), \omega(-\xi, \eta)\}, \quad \Delta \omega(\xi, \eta) = \Delta \omega(-\xi, \eta). \quad (60)$$

To illustrate this result, we solve the vorticity Eq. (56) on the unity square domain with the same boundary velocities as the inviscid cellular flow (i.e., the boundary velocities resulted from Eq. (52)). Consequently, not only the domain but also the velocity magnitude on

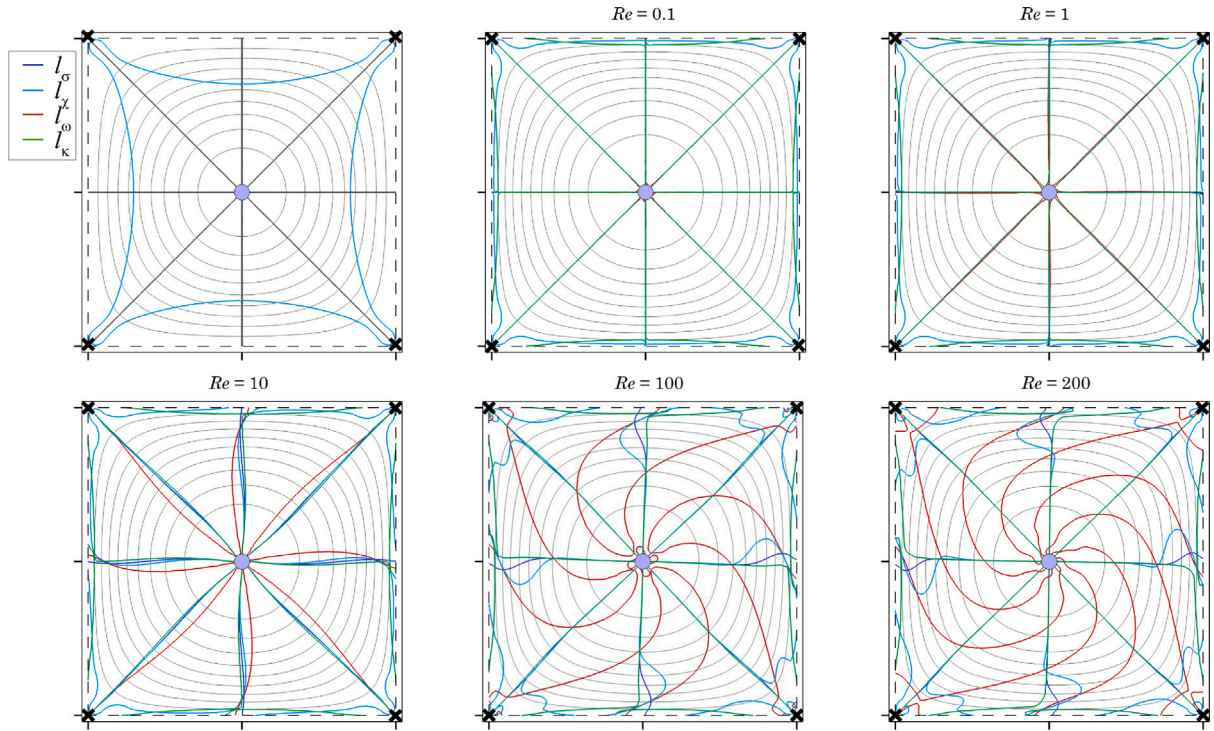


Fig. 8. Streamlines (solid grey lines) and raw feature lines (according to the legend) for the equilateral viscous cellular flows of different Reynolds numbers satisfying the vorticity Eq. (56) with boundary conditions resulting from the inviscid solution (52), on $\Omega = [0, 1] \times [0, 1]$. The inviscid solution is shown on the top left panel. The dashed black lines denote zero streamlines, which form the boundary of the flow field. The black crosses and the blue circles denote the saddles and the extrema, respectively.

the boundary is axisymmetric with respect to the four symmetry axes of the unity square. The streamlines and the raw feature lines are shown in Fig. 8. We show the inviscid (Eulerian) solutions at the top left corners of the figures. The viscous solutions ordered by increasing Reynolds numbers can be seen from the top left to the bottom right corners.

The main topological character of the raw feature line pattern has remained unchanged despite the appearance of viscous dissipation and the raw feature lines of vorticity, l_ω . None of the raw feature lines detached from the central extremum or the saddle points in the corners. However, they separated from the symmetry axes of the domain (which are not symmetry axes of the streamline pattern anymore) and the intersection point with the zero streamlines at the side boundaries, Fig. 8.

A similar conclusion results from the viscous simulations using boundary conditions from the rescaled cellular flow defined by Eq. (54). The separated feature lines stay close to the two symmetry axes of the domain and show a more general picture elsewhere, especially around the broken diagonal symmetry axes Fig. 9. We conclude by comparing Fig. 8 with Fig. 9 that the breaking of the kinematic symmetries of the streamlines has a more significant effect on the separation of the feature lines than the viscous symmetry-breaking has.

We note here some general observations. There is a point symmetry of the feature line patterns with respect to the central extremum point because of the symmetry of the boundary velocity profiles. The deviance of the feature lines according to the viscous dissipation is more significant near the boundaries because the viscous dissipation force is more considerable due to the bigger velocity gradients. There is a specific range in the Reynolds number with which the effect of the viscous dissipation is significant.

Most importantly, the separating effect of the viscous symmetry-breaking is significantly lower than the separating effect of the symmetry-breaking transformations of the boundaries in the raw feature lines, as seen by comparing Figs. 8 and 9 with Figs. 4, 5, 6, or 7. The raw feature line of vorticity, l_ω , has shown the highest sensitivity to the dissipation effects in terms of the separation. This conclusion

is similar for terrain topographies, where the raw feature line of the Laplacian, l_ω , was the most sensitive to the asymmetries of the domain and the isohypse curves.

5. Raw feature line identification in a natural vortex pattern

In this Section, we detect raw feature line patterns in a natural flow characterized by large-scale circulations. In large and shallow lakes with negligible throughflow, circulation is forced by the wind acting on the water surface. Due to the shallowness, the depth-averaged or depth-integrated flow description can be acceptable, resulting in a 2D flow field. We modeled the circulation pattern of Lake Balaton in Hungary by solving the shallow water equations numerically using the Mike21 model by DHI [25]. The depth-averaged approach is applicable for Lake Balaton to estimate the large-scale flow patterns since the mean depth of the lake is 3.2 m while its surface area is 596 km² [26,27]. The numerical solution is obtained by a finite-volume scheme with second-order accurate time integration on a triangular mesh. The cell size increases gradually from 100 m to 500 m from the shoreline to open water zones. We simulate the steady state circulation pattern for the prevailing NNW wind direction with 10 m/s wind speed. The model simulation results in the two horizontal velocity components and the water depth from which streamlines were derived.

In Fig. 10, we see the typical wind-induced, horizontal circulation pattern in Lake Balaton for the prevailing wind. The contours are streamlines associated with depth-integrated velocities, and the warm and cold colors refer to domains with oppositely rotating water. We analyze in detail the raw feature line pattern of the two large-scale gyres that develop and characterize the transport processes of the whole eastern basin. We find the raw feature lines on the numerically obtained streamline field, and we detect the saddle and extremum points by fulfilling the conditions of $\nabla\psi = 0$. In addition, we write out a simple model with continuous functions for each vortex to mimic their circulation patterns similarly to the earlier examples. Although these functions do not satisfy any fluid dynamic equations, they can provide

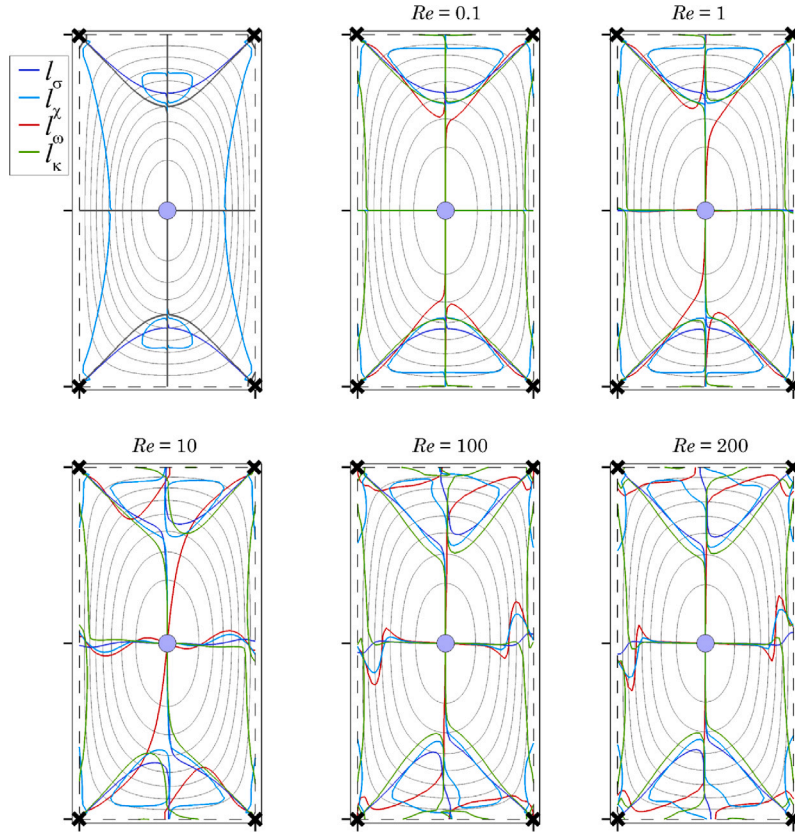


Fig. 9. Streamlines (solid grey lines) and raw feature lines (according to the legend) for the rescaled viscous cellular flows of different Reynolds numbers satisfying the vorticity Eq. (56) with boundary conditions resulting from the inviscid solution (54), on $\Omega = [0, 0.5] \times [0, 1]$. The inviscid solution is shown on the top left panel. The dashed black lines denote zero streamlines, which form the boundary of the flow field. The black crosses and the blue circles denote the saddles and the extrema, respectively.

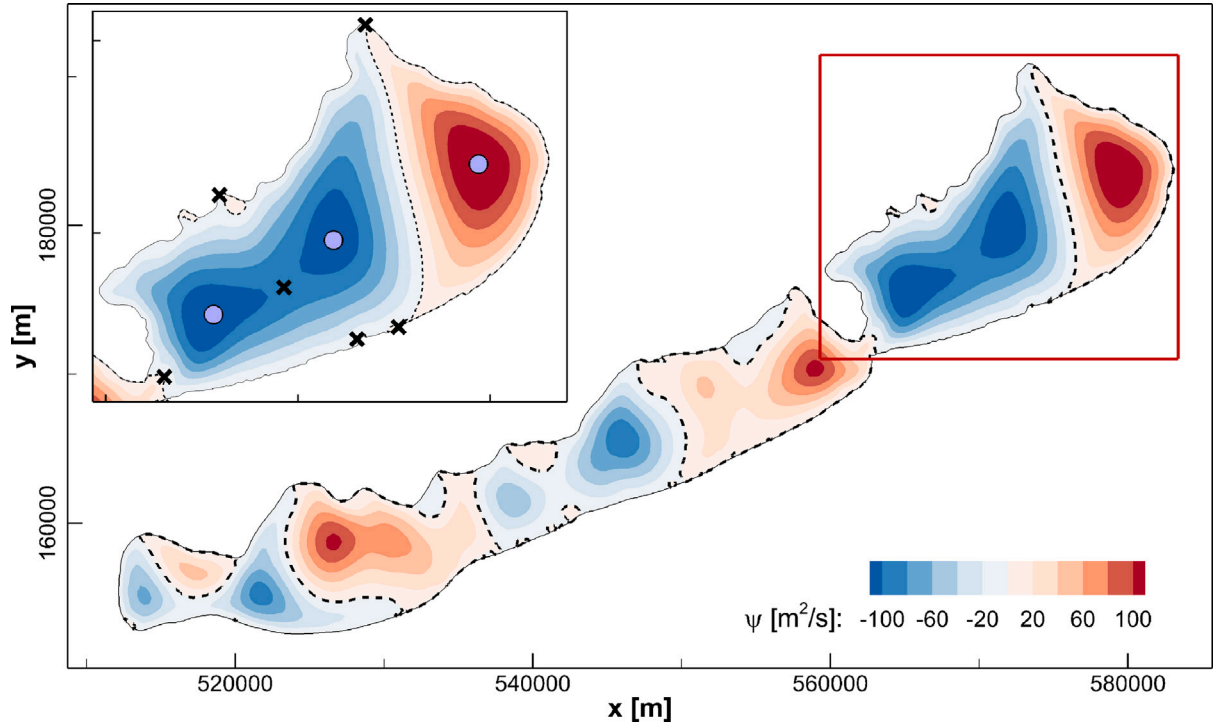


Fig. 10. The simulated depth-integrated circulation pattern in Lake Balaton for the prevailing NNW wind direction. The geographical (Cartesian) coordinates are in a meter unit distance. The contours are streamlines. Warm and cold colors refer to clockwise and counterclockwise circulations, respectively, while the dashed black lines are zero streamlines that separate the oppositely rotating subdomains. The analyzed eastern basin is enlarged on the subpanel, showing the saddles (black crosses) and extrema (blue circles).

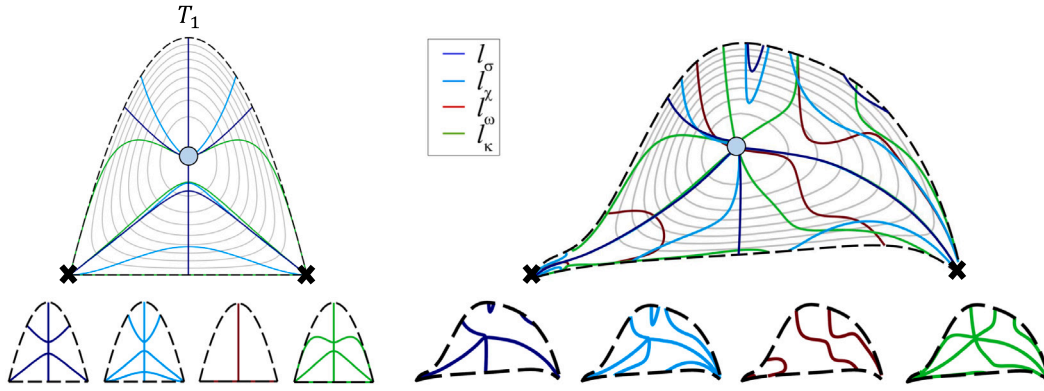


Fig. 11. Streamlines (solid grey lines) and raw feature lines (according to the legend) for a symmetric, arch-shaped vortex and its asymmetric deformation as a kinematic model of the vortex on the right side of the eastern basin of Lake Balaton. The dashed black lines denote zero streamlines, which form the boundary of the vortices. The black crosses and the blue circles denote the saddles and the extrema, respectively.

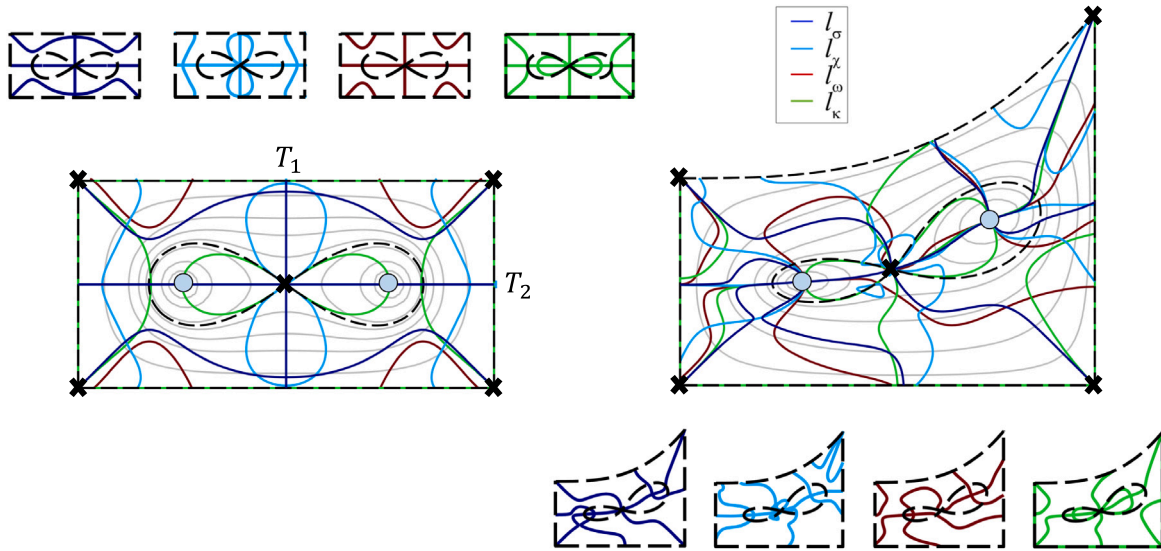


Fig. 12. Streamlines (solid grey lines) and raw feature lines (according to the legend) for a symmetric, rectangular vortex with two extrema and five saddles and its asymmetric deformation as a kinematic model of the vortex on the left side of the eastern basin of Lake Balaton. The dashed black lines denote zero streamlines, which form the boundary of the vortices, and nonzero streamlines that cross the central saddle and turn around the extrema. The black crosses and the blue circles denote the saddles and the extrema, respectively.

guidance to map and understand the evolution of the raw feature lines within a natural environment. More precisely, they help explore the role of the kinematic and dynamic constraints for each feature line.

The first vortex – the one on the right of the zoomed picture in Fig. 10 – has an extremum and two saddles with curved boundaries. The longer part of the boundary is the shore of the lake. The remaining is the zero streamline that separates the vortex from the neighboring one. We describe this vortex with a prototype constructed by the product of the implicit curves describing the boundary. First, we start from a symmetric vortex from which the prototype will be unfolded. This is an arch-based domain with one symmetry axis, as shown on the left panel of Fig. 11. The equation of the streamlines and the coinciding condition of the raw feature lines read as

$$\begin{aligned} \psi &= y(y + 4x(x - 1)), \\ T_1 &= l_\sigma \cap l_\chi \cap l_\omega \cap l_k. \end{aligned} \quad (61)$$

We describe the eastern vortex of Lake Balaton by generalizing the previous one as

$$\psi = (y - P_1(x))(y - P_2(x)), \quad (62)$$

where $P_1(x)$ and $P_2(x)$ are polynomials of degree six and nine, respectively. The polynomials were fitted to certain points extracted from the

numerical streamline field and transformed so that the x axis fits the two saddle points.

The second chosen vortex has two subregions that rotate in the same direction and are separated by a saddle. Some streamlines surround the two vortex cores and form a common outer region bounded by the lake shore and zero streamlines. In the left panel of Fig. 12, we show a scalar field with two extrema, five saddles, and two symmetry axes. The equation of the streamlines and the coinciding condition of the raw feature lines are

$$\begin{aligned} \psi &= xy(x - 2)(y - 1) \\ &\left(\frac{1}{\sqrt{(x - 0.5)^2 + (y - 0.5)^2}} + \frac{1}{\sqrt{(x - 1.5)^2 + (y - 0.5)^2}} \right), \\ T_1 \cup T_2 &= l_\sigma \cap l_\chi \cap l_\omega \cap l_k. \end{aligned} \quad (63)$$

The prototype of the second vortex of Lake Balaton is unfolded from the stream function above as

$$\begin{aligned} \psi &= xy(x - 2)(y - 0.1x^3 - 1) \\ &\times \left(\frac{1}{\sqrt{\frac{(x - 0.5 - 0.2y)^2}{4} + (y - 0.5)^2}} + \frac{1}{\sqrt{\frac{(x - 1.5)^2}{4} + \frac{(y - 0.5 - 0.2x)^2}{2}}} \right). \end{aligned} \quad (64)$$

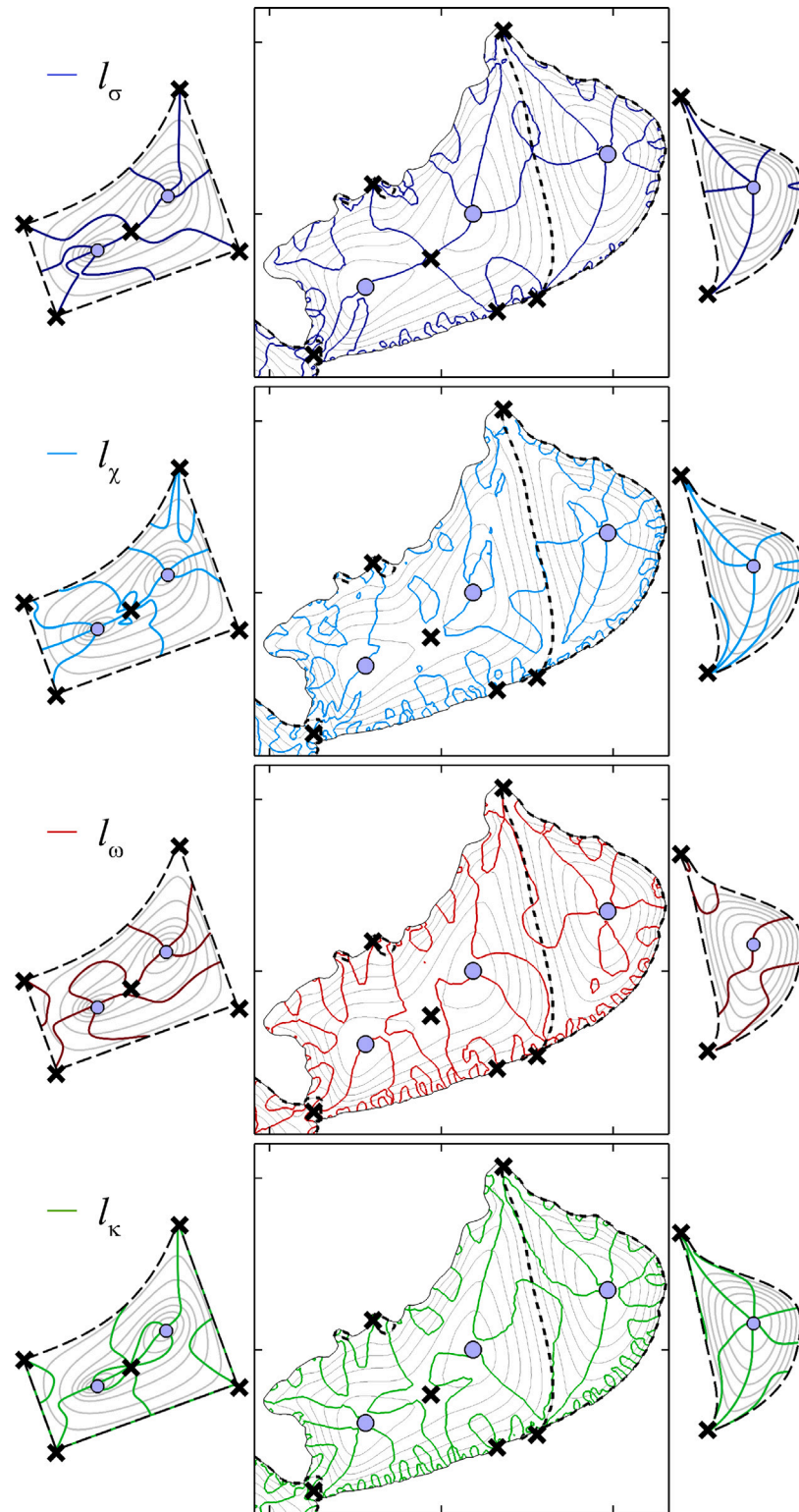


Fig. 13. Streamlines (solid grey lines) and raw feature lines (according to the legend) for the two vortex formations of the eastern basin of Lake Balaton. The corresponding kinematic prototype vortices are placed on the left and right sides. The dashed black lines denote zero streamlines (vortex boundaries). The black crosses and the blue circles denote the saddles and the extrema, respectively.

As seen in the right panel of Fig. 12, the number of saddles and extrema is unchanged. The symmetry axes have broken due to the transformation of the northern side of the rectangular boundary into a cubic curve and the deformation and rotation of the inner circular domains.

The streamlines and the raw feature lines are based on the prototype models defined by Eqs. (62) and (64), and the results of the numerical model are shown in Fig. 13. The raw feature line pattern of the velocity magnitude l_σ and contour curvature l_κ shows good correspondence between the results of the toy models and the simulations. The effect of viscous dissipation and eddy viscosity is included in the numerical simulations. However, their effect is not significant compared to the kinematic constraints.

To conclude, the primary influence that affects the raw feature line pattern in a large-scale domain of vortices is the shape of the domain, especially the shape of the bounding curve of the domain. Some subsets of the raw feature lines connect the saddles, the extrema, and the boundaries of the vortices similarly to the terrain examples seen in Figs. 5 and 6, and the vortex prototype models in Figs. 11 and 12. We observe fine patterns of feature lines around the shoreline of Lake Balaton, which appear only in the numerical solutions. These patterns also result from the shoreline geometry, as it is small-scale details appear in the model of the lake basin. Finally, the sensitivity of the raw feature lines of vorticity, l_ω , is higher in the natural example as well, as we have seen in the previous Sections on terrain and general fluid mechanical models.

6. Concluding remarks

We developed a condition on the coincidence of the raw feature lines of slope (velocity magnitude) and contour curvature (streamline curvature), which involved the coincidence of the raw feature lines of second-order slope (velocity gradient magnitude) and Laplacian (vorticity) as well, Theorem 2. We also deduced a sufficient condition on the coinciding extremal lines along the symmetry axes of the contour lines (streamlines), Theorem 3. The results have been applied to describe simple, symmetric, and asymmetric terrain fields, ideal and viscous cellular flows, and large-scale environmental vortex patterns.

The effect of the geometric (kinematic) symmetries turned out to be more significant compared to the viscous effects in the fluid mechanical examples. The raw feature line of the Laplacian (vorticity), l_ω , showed the highest separation rates and sensitivity to the symmetry-breaking transformations. This is a common feature of the terrain and fluid flow models, even though the fluid mechanical models include a 2D vorticity transport equation (cellular flows) or a pair of depth-integrated shallow water momentum equations (environmental flow model of Lake Balaton) as a dynamic constraint. The raw feature line l_ω can refer to the extremal convergence or divergence of the slope lines of a terrain map and the extremal vorticity – in other words, the extremal local angular velocity of the fluid elements – of a planar fluid flow field. In this way, we can describe terrain maps by using l_ω and speak, for example, about an ideal terrain object with the absence of l_ω and extremal slope lines (similarly, ideal fluid flows do not have l_ω extremal vorticity lines). On the other hand, the coincidence of the raw feature lines and extremal lines describes line-like objects in both terrain and fluid flow fields. The coincidence of the extremal slope with the extremal contour curvature (or extremal velocity magnitude with the extremal streamline curvature) usually also involves the coincidence of the extremal second-order slope and the extremal Laplacian (or extremal velocity gradient magnitude and extremal vorticity). Whether the model is a terrain map or a planar fluid flow field, geometric circumstances determine primarily the pattern of raw features.

CRediT authorship contribution statement

Balázs Sándor: Conceptualization, Data curation, Formal analysis, Investigation, Methodology, Software, Visualization, Writing – original draft, Writing – review & editing. **Péter Torma:** Conceptualization, Data curation, Funding acquisition, Methodology, Project administration, Resources, Software, Supervision, Validation, Visualization.

Declaration of competing interest

The authors declare that they have no known competing financial interests or personal relationships that could have appeared to influence the work reported in this paper.

Data availability

Data will be made available on request.

Acknowledgments

The research was funded by the Sustainable Development and Technologies National Programme of the Hungarian Academy of Sciences (FFT NP FTA). The research presented in the article was carried out within the framework of the Széchenyi Plan Plus program with the support of the RRF 2.3.1 21 2022 00008 project. This research was also funded by the Ministry of Culture and Innovation and the National Research, Development and Innovation Office under Grant Nr. TKP2021-NVA-02. Finally, funding was also provided by the Hungarian Academy of Sciences (Grant Number : János Bolyai fellowship 00906/23).

References

- [1] A. Cayley, On contour and slope lines, Lond. Edinb. Dublin Philos. Mag. J. Sci. 18 (1859) 264–268, <http://dx.doi.org/10.1080/14786445908642760>.
- [2] J.C. Maxwell, On Hills and dales, Philos. Mag. Ser. 4 (40) (1870) 421–427, <http://dx.doi.org/10.1080/14786447008640422>.
- [3] R. Peikert, F. Sadlo, Height ridge computation and filtering for visualization, in: Conference: Visualization Symposium, PacificVis '08, IEEE Pacific, 2008, <http://dx.doi.org/10.1109/PACIFICVIS.2008.4475467>.
- [4] S. Bonetti, A.D. Bragg, A. Porporato, On the theory of drainage area for regular and non-regular points, Proc. R. Soc. Lond. Ser. A Math. Phys. Eng. Sci. 474 (2018) 20170693, <http://dx.doi.org/10.1098/rspa.2017.0693>.
- [5] R. Peikert, M. Roth, The parallel vectors operator-a vector field visualization primitive, in: Proceedings Visualization '99 (Cat. No. 99CB37067), <http://dx.doi.org/10.1109/VISUAL.1999.809896>.
- [6] J.J. Koenderink, A.J. van Doorn, Two-plus-one-dimensional differential geometry, Pattern. Recognit. Lett. 15 (1994) 439–443, [http://dx.doi.org/10.1016/0167-8655\(94\)90134-1](http://dx.doi.org/10.1016/0167-8655(94)90134-1).
- [7] M. de Saint-Venant, Surfaces à plus grande pente constituées sur des lignes courbes, Bull. Soc. Philomath. Paris (1852) 24–30.
- [8] T. Lindeberg, Edge detection and ridge detection with automatic scale selection, Int. J. Comput. Vis. 30 (2) (1998) 117–156.
- [9] D.N. Kenwright, Automatic detection of open and closed separation and attachment lines, in: Proceedings Visualization '98 (Cat. No. 98CB36276), <http://dx.doi.org/10.1109/VISUAL.1998.745297>.
- [10] M. Gauding, et al., On the self-similarity of line segments in decaying homogeneous isotropic turbulence, Comput. & Fluids 180 (2019) 206–217, <http://dx.doi.org/10.1016/j.compfluid.2018.08.001>.
- [11] L. Wang, N. Peters, The length-scale distribution function of the distance between extremal points in passive scalar turbulence, J. Fluid Mech. 554 (2006) 457–475, <http://dx.doi.org/10.1017/S0022112006009128>.
- [12] S.C. Shadden, F. Lekien, J.E. Marsden, Definition and properties of Lagrangian coherent structures from finite-time Lyapunov exponents in two-dimensional aperiodic flows, Physica D 212 (2005) 271–304, <http://dx.doi.org/10.1016/j.physd.2005.10.007>.
- [13] G. Haller, A variational theory of hyperbolic Lagrangian coherent structures, Physica D 240 (2011) 574–598, <http://dx.doi.org/10.1016/j.physd.2010.11.010>.
- [14] L. Zhang, et al., Flow visualization based on a derived rotation field, Electron. Imaging (1) (2016) 1–10, <http://dx.doi.org/10.2352/ISSN.2470-1173.2016.1.VDA-478>.
- [15] J.Z. Wu, et al., A vorticity dynamics theory of three-dimensional flow separation, Phys. Fluids A 12 (2000) 1932–1954.

- [16] A. Surana, O. Grunberg, G. Haller, Exact theory of three-dimensional flow separation. Part 1. Steady separation, *J. Fluid Mech.* 564 (2006) 57–103, <http://dx.doi.org/10.1017/S0022112006001200>.
- [17] H. Miura, S. Kida, Identification of tubular vortices in turbulence, *J. Phys. Soc. Japan* 66 (1997) 1331–1334, <http://dx.doi.org/10.1143/JPSJ.66.1331>.
- [18] F. Sadlo, R. Peikert, M. Sick, Visualization tools for vorticity transport analysis in incompressible flow, *IEEE Trans. Vis. Comput. Graphics* 12 (5) (2006) 949–956, <http://dx.doi.org/10.1109/TVCG.2006.199>.
- [19] J. Sahnner, T. Weinkauff, H.C. Hege, Galilean invariant extraction and iconic representation of vortex core lines, in: *EUROGRAPHICS - IEEE VGTC Symposium on Visualization*, 2005, <http://dx.doi.org/10.2312/VisSym/EuroVis05/151-160>.
- [20] G. Haller, An objective definition of a vortex, *J. Fluid Mech.* 525 (2005) 1–26, <http://dx.doi.org/10.1017/S0022112004002526>.
- [21] C. Wiener, *Lehrbuch der darstellenden Geometrie*, vol. 2, Leipzig, 1887.
- [22] R. Goldman, Curvature formulas for implicit curves and surfaces, *Comput. Aided Geom. Design* 22 (2005) 632–658, <http://dx.doi.org/10.1016/j.cagd.2005.06.005>.
- [23] V.K. Andreev, *Applications of Group-Theoretical Methods in Hydrodynamics*, Springer Dordrecht, 1998,2013, <http://dx.doi.org/10.1007/978-94-017-0745-9>.
- [24] V.I. Arnold, *Mathematical Methods of Classical Mechanics*, Springer, New York, NY, 1978,2013, <http://dx.doi.org/10.1007/978-1-4757-1693-1>.
- [25] Y. Li, Q. Zhang, J. Yao, A.D. Werner, X. Li, Hydrodynamic and hydrological modelling of the Poyang lake catchment system in China, *J. Hydrol. Eng.* 19 (3) (2014) 607–616.
- [26] Mihály Kocsis, Gábor Szatmári, Pirooska Kassai, et al., Soluble phosphorus content of lake balaton sediments, *J. Maps* 18 (2) (2022) 142–150, <http://dx.doi.org/10.1080/17445647.2021.2004943>.
- [27] B. Sándor, P. Torma, K.G. Szabó, et al., Interaction between depth variation and turbulent diffusion in depth-averaged vorticity equations, *Theor. Comput. Fluid Dyn.* (2023) <http://dx.doi.org/10.1007/s00162-023-00665-y>.